J. Fluid Mech. (1979) *vol.* 91, *part* 4, *pp.* 679–696
Printed in Great Britain

Ionizing argon boundary layers. Part 2. Shock-tube side-wall boundary-layer flows

By W. S. LIU† AND I. I. GLASS
Institute for Aerospace Studies, University of Toronto, Ontario, Canada M3H 5T6

(Received 10 August 1978)

A combined experimental and theoretical investigation was conducted on the shock-tube side-wall ionizing boundary-layer induced by a shock wave moving into argon. The dual-wavelength interferometric boundary-layer data were obtained by using a 23 cm diameter Mach–Zehnder interferometer with the 10×18 cm Hypervelocity Shock Tube at initial shock Mach numbers of 13 and 16, an initial pressure of 5 torr and a temperature of 300 °K. The plasma density and electron number density in the boundary layer were measured and compared with numerical profiles obtained by using an implicit finite-difference scheme for a two-temperature, chemical non-equilibrium, laminar boundary-layer flow in ionizing argon. The analysis included the variations of transport properties based on elastic-scattering cross-sections, effects of chemical reactions, radiation-energy losses and electron-sheath wall boundary conditions. Considering the difficulties involved in such complex plasma flows, satisfactory agreement was obtained between the analyses and experiments. A comparison was made with the flat-plate case and despite the very different velocity boundary conditions at the wall for the two flows the experimental data appear to be quite similar. The experimental bump in the profile of electron number density which was found in the flat-plate case was not found in the side-wall case. Comparisons and discussions of the results for the different types of boundary layer are presented, including a comparison between experimentally derived and analytical plasma-temperature profiles.

1. Introduction

During the past decade a number of investigations have been made of ionizing boundary-layer flows. Vehicles travelling at high speed generate ionized species in the boundary layer which interfere with the transmission of electromagnetic signals to and from the spacecraft. The success of onboard measurements of the maximum or boundary-layer-edge charged-species density on re-entry vehicles depends on the accuracy of boundary-layer theory in predicting their distributions. The shock tube is an important research facility for studying ionizing boundary-layer flows.

Several analyses exist on partially ionized boundary-layer flows (see Liu, Whitten & Glass 1978 for details). Most of these analyses are based on the assumption that the flow is either in thermal equilibrium or chemically frozen. The investigations include stagnation-point, thermal–Rayleigh and flat-plate boundary layers in an ionizing gas. However, the problem of an ionizing non-equilibrium shock-tube side-wall boundary layer induced behind a moving shock wave has received less attention.

† Present address: Thermalhydraulics Research Branch, Whiteshell Nuclear Research Establishment, AECL, Pinawa, Manitoba, Canada R0E 1LO.

0022-1120/79/4186-6190 $02.00

Nevertheless, the shock-tube side-wall boundary layer has important effects on ionizing shock-wave structure and flat-plate boundary layers.

As shown by Mirels (1966), the flow between the shock wave and the contact surface in an actual shock tube is non-uniform owing to the growth of the shock-tube side-wall boundary layer. The gross features of shock-wave structure in an ionizing gas are affected by the side-wall boundary layer. This type of layer was investigated by Knōōs (1968) for flows in thermal and chemical equilibrium. He showed that near the wall the flow is in non-equilibrium or near frozen. Therefore equilibrium solutions are not valid. Honma & Komuro (1976) concluded that the thickness of the electron thermal layer is an order greater than that of the viscous boundary layer based on a frozen-flow assumption. A side-wall boundary-layer flow in thermal and chemical non-equilibrium flow was analysed by Takano & Akamatsu (1975). All of these investigations neglected radiation-energy losses. However, for boundary-layer flows generated by strong shock waves ($M_s > 13$), the radiative processes are very important and cannot be neglected in either the inviscid or the boundary-layer flow regions.

Experimental investigations on ionizing boundary-layer flows are relatively scarce. Flat-plate boundary-layer electron-temperature measurements were made by Brown & Mitchner (1971) in a seeded argon plasma using a spectroscopic technique. Ion-density profiles in supersonic boundary layers over a flat plate in shock-heated air were measured by Bredfeldt *et al.* (1967) by using flush-mounted electrostatic probes. The agreement between their experimental data and analysis was inconclusive, owing either to the approximations made in the theoretical models or to the uncertainty involved in the diagnostic technique. Free-molecule cylindrical Langmuir probes were used by Tseng & Talbot (1971) to measure distributions of charged-particle density, electron temperature and plasma potential in a flat-plate boundary layer. Similarity solutions compared favourably with experimental results for profiles of charged-particle density and electron temperature. All these experiments were done in flows at relatively low temperatures and low electron number densities. In this domain, the radiation-energy loss is very small and can be neglected in both the inviscid and the viscous flow region. The edge conditions for the boundary layers were calculated from non-radiant models. Recently, profiles of electron number density in ionizing flat-plate boundary-layer flows generated by a strong shock wave were measured interferometrically (Whitten 1978) by using the UTIAS 10×18 cm Hypervelocity Shock Tube at shock Mach numbers $M_s \sim 13$ and 16 at an initial argon pressure $p_0 \sim 5$ torr. Satisfactory to good agreement was obtained (Liu *et al.* 1978) between analysis and experiment. For a thermal–Rayleigh boundary layer, Kuiper (1968) measured the profile of electron number density for ionizing argon boundary-layer flows at $M_s = 11{\cdot}1$ and $p_0 = 5$ torr. However, except for Brimelow's (1974) results, there were no data on shock-tube side-wall boundary-layer flows.

The main differences between the analyses for flat-plate and shock-tube side-wall boundary layers are as follows;

(i) The velocity profile for the flat-plate case increases from zero at the wall to the free-stream value at the edge of the boundary layer. For the side-wall boundary layer, however, the velocity profile decreases from the shock speed at the wall to the free-stream value at the edge in steady-flow co-ordinates attached to the shock wave.

(ii) Ionizing non-equilibrium phenomena occur in the free-stream flow behind the shock front. Consequently, the variations of the free-stream conditions for the side-wall boundary layer are significantly greater than for a flat plate, especially in the regions of the ionizing shock structure and beyond, where radiation losses are large.

In part 1 of this research (Liu *et al.* 1978), two-temperature chemically non-equilibrium, laminar, flat-plate boundary-layer flows in ionizing argon were solved by an implicit finite-difference scheme. That analysis extended previous work by considering the radiation-energy loss and the appropriate chemical reactions in the ionizing boundary-layer and free-stream flows. It included the variations in transport properties, effects of chemical reactions, radiation-energy loss and the electric-sheath wall boundary conditions. The results were compared with dual-wavelength interferometric data for flat-plate boundary-layer flows.

The present research deals with measurements and related analyses of the profiles of total plasma density and the electron number density in shock-tube side-wall boundary-layer flows under initial conditions close to those used in the flat-plate cases for ready comparison. The model of shock-wave structure of Glass & Liu (1978), which includes radiation-energy losses, was used and Brimelow's (1974) interferometric data were re-evaluated for comparison with the present analysis and with the flat-plate cases. Experimentally derived plasma temperature profiles are also compared with analysis. Satisfactory to good agreement has been obtained with the experimental data. It is possible that even better agreement will be obtained with the accurate interferometric data in the future when improved analytical models have been developed. However, considering the complexity of the problem the results are very reasonable.

2. Theoretical aspects

In part 1 of this work (Liu *et al.* 1978) details were given of the theoretical considerations for ionizing-argon boundary-layer flows. A brief description of the analysis is provided here. The boundary-layer equations for a two-temperature, chemically non-equilibrium, ionizing gas are transformed into similarity form to make them more suitable for numerical analysis. The independent variables are

$$\xi(x) = \int_0^x \rho_\delta \mu_\delta u_\delta \, dx, \quad \eta(x,y) = \frac{u_\delta}{(2\xi)^{\frac{1}{2}}} \int \rho \, dy, \tag{1}$$

where x is the co-ordinate along the surface and y is normal to it, while u and ρ are the velocity in the x direction and total density of the plasma, respectively. Subscript δ denotes the edge of boundary layer.

The basic equations are transformed from x, y to ξ, η co-ordinates. The transformed equations for momentum, electron species, atom temperature and electron temperature are

$$[Cf'']' + ff'' + \beta_f \left[\frac{\rho_\delta}{\rho} - f'^2\right] = 2\xi \left[f' \frac{\partial f'}{\partial \xi} - \frac{\partial f}{\partial \xi} f''\right], \tag{2}$$

$$\left[\frac{C}{Sc} z'\right]' + fz' - \beta_z z f' + \frac{2\xi}{\rho_\delta \mu_\delta u_\delta^2} \frac{m_a \dot{n}_e}{\rho \alpha_\delta} = 2\xi \left[f' \frac{\partial z}{\partial \xi} - \frac{\partial f}{\partial \xi} z'\right], \tag{3}$$

$$\left[\frac{C}{Pr}\theta'\right]' + f\theta' + \frac{u_\delta^2}{C_p T_{a\delta}} Cf''^2 - \beta_{T_a}\theta f' - \beta_f \frac{u_\delta^2}{C_p T_{a\delta}} \frac{\rho_\delta}{\rho} f' - \frac{2\xi}{\rho_\delta \mu_\delta u_\delta^2} \frac{Q_{el} + k_B T_I (\dot{n}_e)_a + Q_R}{\rho C_p T_{a\delta}} = 2\xi \left[f' \frac{\partial\theta}{\partial\xi} - \frac{\partial f}{\partial\xi}\theta'\right], \tag{4}$$

$$\left[\frac{C}{Pr_e}\Theta'\right]' + \frac{C}{Sc}\alpha_\delta z'\Theta' + \alpha_\delta z f\Theta' - \beta_{T_e}\alpha_\delta z f'\Theta + \frac{2\xi}{\rho_\delta \mu_\delta u_\delta^2} \frac{Q_{el} - (k_B T_I + \frac{5}{2}k_B T_e)(\dot{n}_e)_e - \frac{5}{2}k_B T_e (\dot{n}_e)_a}{\rho C_p T_{e\delta}} = 2\xi\alpha_\delta z \left[f' \frac{\partial\Theta}{\partial\xi} - \frac{\partial f}{\partial\xi}\Theta'\right], \tag{5}$$

where a prime denotes $\partial/\partial\eta$ and the following definitions have been used:

$$f' = \frac{u}{u_\delta}, \quad \Theta = \frac{T_e}{T_{e\delta}}, \quad z = \frac{\alpha}{\alpha_\delta}, \quad C = \frac{\rho\mu}{\rho_\delta \mu_\delta},$$

$$\theta = \frac{T_a}{T_{a\delta}}, \quad Sc = \frac{\mu}{\rho D_a}, \quad Pr = \frac{\mu C_p}{\lambda_a + \lambda_i}, \quad Pr_e = \frac{\mu C_p}{\lambda_e},$$

$$\beta_f = \frac{2\xi}{u_\delta}\frac{du_\delta}{d\xi}, \quad \beta_{T_a} = \frac{2\xi}{T_{a\delta}}\frac{dT_{a\delta}}{d\xi},$$

$$\beta_z = \frac{2\xi}{\alpha_\delta}\frac{d\alpha_\delta}{d\xi}, \quad \beta_{T_e} = \frac{2\xi}{T_{e\delta}}\frac{dT_{e\delta}}{d\xi}.$$

Here T is the temperature, α the degree of ionization, μ the plasma viscosity coefficient, D_a the ambipolar-diffusion coefficient, C_p the frozen specific-heat capacity, λ the thermal-conductivity coefficient, m_a the gas atomic mass, $\dot{n}_e$ the electron-number-density production rate, Q_{el} the elastic energy-transfer rate to free electrons, Q_R the plasma radiation energy-loss rate, which consists of continuum-radiation and line-radiation losses, k_B is the Boltzmann constant and the subscripts a, e and I denote atom, electron and ionization, respectively.

Solutions are strongly dependent on the models used in the descriptions of the elastic and inelastic energy-transfer rates, radiation-energy losses, chemical-reaction rates and plasma-transport properties. The elastic-scattering cross-sections between each pair of species are used in the determination of the elastic-energy transfer rate and transport properties. They can be evaluated from experimental results or from scattering theory. Inelastic-scattering cross-sections between atoms and atoms and between atoms and electrons are required in the calculation of electron-production rates. Details of these scattering cross-sections in an argon plasma, basic assumptions, boundary conditions and initial conditions are described in part 1.

The solutions for u_δ, $T_{a\delta}$, $T_{e\delta}$, α_δ and p_δ were obtained from a model of shock-wave structure (Glass & Liu 1978) which includes the radiation-energy losses but neglects the effects of the side-wall boundary layer on the shock-wave structure. (This interaction has now been solved and will be reported at a later date.) The initial profiles at the leading edge are calculated from the ordinary differential equations with two-point boundary conditions.

The nonlinear partial differential equations (2)–(5), with boundary conditions of a mixed Neumann and Dirichlet type, were solved numerically by an implicit six-point finite-difference scheme. The momentum equation was solved first and the species

equation was solved before the atom- and electron-temperature equations. The linearized equations were written in the following common form:

$$x_1 W_{\eta\eta} + x_2 W_\eta + x_3 W = x_4 W_\xi + x_5, \tag{6}$$

where $W = F$, z, θ and Θ, $F = \partial f/\partial\eta$ and the x_i are the coefficients.

The linearized equations are of second order and were solved in order for the unknowns F, z, θ and Θ. The derivatives and the integral in the η direction were then expressed as three-point difference formulae. The derivatives in the ξ direction were approximated by a backward-difference scheme. When these different quotients and expressions were used with the partial differential equations (2)–(5), the finite-difference equations became simultaneous linear algebraic equations:

$$A_i W_{i-1,j+1} + B_i W_{i,j+1} + C_i W_{i+1,j+1} = D_i, \tag{7}$$

where i and j are the indices of the η, ξ co-ordinates for the difference net at the point considered while A_i, B_i, C_i and D_i are the matrix elements. These tridiagonal matrix equations were solved by the Thomas algorithm.

The computational scheme is an iterative one. The momentum equation is first solved with assumed profiles of species and atom and electron temperatures. The resulting velocity field is employed for the other equations. The resulting species is then used for the atom temperature, and subsequently for the electron-temperature equation. The new species and atom- and electron-temperature profiles are then used to replace the assumed ones and the process continues until the solutions converge to satisfy a preset criterion. In general it takes three iterations for a flat-plate boundary layer and six iterations for a side-wall boundary layer to reach errors within 10^{-4}. It is worth noting that the step size Δx used for the side-wall boundary layer is much smaller than that for the flat-plate case and results in increased computation time. The strategy of the step-size control on x at the $j+1$ step is as follows:

$$\Delta x_{j+1} = c_{j+1}\,\delta_j^*, \tag{8}$$

where δ^* is the boundary-layer displacement thickness and the control constant c_{j+1} is given by

$$c_{j+1} = f[c_j, \text{ iteration number, } \max(|W_{i,j} - W_{i,j-1}|)].$$

In general, Δx_{j+1} is strongly dependent on the variations of the free-stream flow properties.

3. Experimental aspects

The present experiments were conducted in the UTIAS combustion-driven 10×18 cm Hypervelocity Shock Tube. A Mach–Zehnder interferometer with a 23 cm diameter field of view, using a pulsed laser light source, was the main diagnostic instrument. Since the original construction of the facility (Boyer 1965), several modifications have been made which have substantially improved the performance and ease of handling. The details are described by Bristow (1971), Brimelow (1974), Tang (1977), Glass, Liu & Tang (1977), Glass & Liu (1978) and Whitten (1978).

The interferometer had a pulsed (30 ns) ruby-laser light source capable of taking two simultaneous interferograms at 3471·5 Å and 6943 Å. From these it was possible

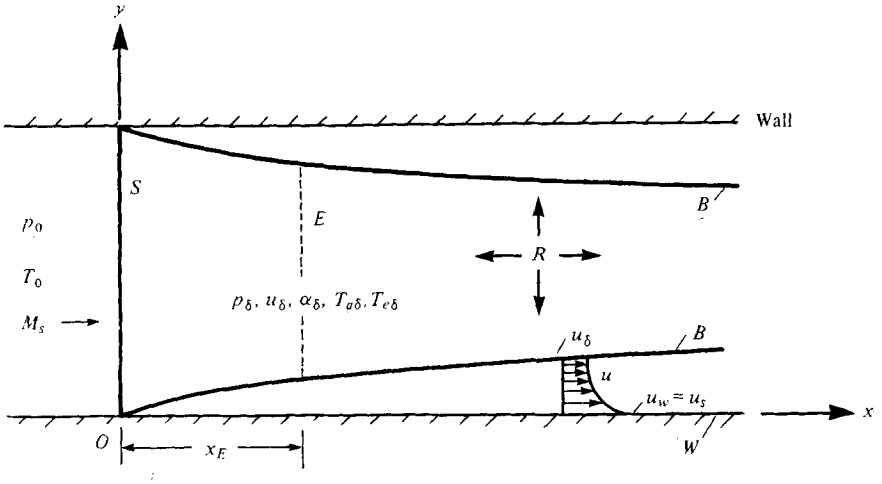

FIGURE 1. Schematic diagram of shock-tube side-wall boundary layer generated by a shock wave moving to the left into a rest state (O). The shock wave S becomes fixed at $x = 0$ by mathematically superposing a counterflow u_s equal to the shock velocity. As a result, the wall now moves to the right at the shock speed u_s. The flow quantities at the edge of the boundary layer have the subscript δ. E denotes the electron-cascade front, R the radiation-cooling zone, B the side-wall boundary layer, W the shock-tube wall.

to determine the electron number density and total plasma density throughout the flow (Glass *et al.* 1977; Glass & Liu 1978).

Accurate measurements of shock velocities are necessary in order to provide precise shock Mach numbers for the numerical calculations. Measurements of shock velocity were obtained between a reference station and four positions along the tube using standard piezoelectric pressure transducers whose outputs were amplified before being applied to two Hewlett-Packard (type 3734A) and two Racal electronic counters measuring in μs units. A fifth velocity measurement was taken across 61 cm of the test section using a Hewlett-Packard (type 5325A) counter measuring in 0·1 μs units. A Kistler (601B) pressure transducer was used to record the pressure across the shock wave and in the induced flow.

Basically, an interferogram consists of bright and dark fringes. Sequential numbers are assigned to the fringes and this gives a relative measurement of the refractive index between a reference and an unknown region. Measurements of fringe shift (i.e. the displacement of a fringe between the undisturbed gas and the regions of reasonably uniform flow behind the front) were substituted into the interferometric equations for ρ and n_e (Glass & Liu 1978). Consequently, α can be calculated from ρ and n_e throughout the entire flow field.

Figure 1 shows schematically the experimental generation of a shock-tube side-wall boundary-layer flow. Figure 2 (plate 1) shows a representative interferogram at 6943 Å of an induced side-wall boundary layer in the radiation-cooling region for $M_s = 15{\cdot}9$, $p_0 = 5{\cdot}1$ torr and $T_0 = 298\,^\circ$K (case 2 in the next section). The complementary interferogram at 3471·5 Å is omitted for brevity as it provides no further visual information. The boundary-layer development along the wall from the translational shock front can be readily seen.

Cases	M_s	p_0 (torr)	T_0 (°K)	u_δ (cm/s)	$T_{a\delta}$ (°K)	$T_{e\delta}$ (°K)	α_δ	p_δ (Pa)	x_m (cm)
1	13·1	5·16	300	$0{\cdot}72\times10^5$	11460	11460	0·061	$0{\cdot}164\times10^6$	9·5
2	15·9	5·10	298	$0{\cdot}52\times10^5$	11040	11040	0·037	$0{\cdot}258\times10^6$	18

TABLE 1. Initial conditions and free-stream conditions in argon at x_m for side-wall boundary-layer flows.

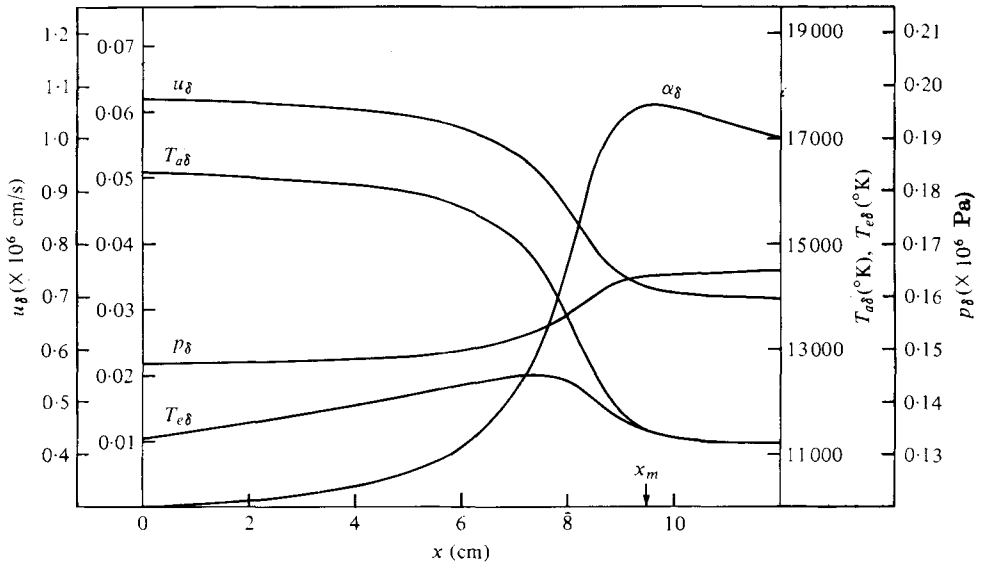

FIGURE 3. Variations of free-stream conditions with distance x for the side-wall boundary-layer flow at $M_s = 13{\cdot}1$, $p_0 = 5{\cdot}16$ torr and $T_0 = 300$ °K. Note in this case $x_m \simeq x_E$.

4. Comparisons and discussions

Recently, Brimelow's data were re-evaluated and compared with the results from the radiant shock-structure model of Glass & Liu. The experimental data show that (i) there is no bump in the profile of electron number density in the side-wall boundary-layer case and (ii) significant two-dimensional effects on the free-stream flow exist in the side-wall layer.

Results for shock-tube side-wall boundary-layer flows

Shock-tube side-wall boundary-layer flows in ionizing argon were studied for $M_s = 13{\cdot}1$, $p_0 = 5{\cdot}16$ torr (case 1) and $M_s = 15{\cdot}9$ and $p_0 = 5{\cdot}1$ torr (case 2) at 300 °K. The initial conditions for these two cases are nearly identical with those for the two flat-plate boundary layers studied in part 1. The initial conditions and the free-stream conditions at the measuring station x_m are given in table 1.

The free-stream conditions calculated from the radiant shock-structure model for case 1 are plotted in figure 3. The measuring station x_m is located nearly at the electron-cascade front, where the electron number density is a maximum and the radiation process starts to influence the downstream cooling zone.

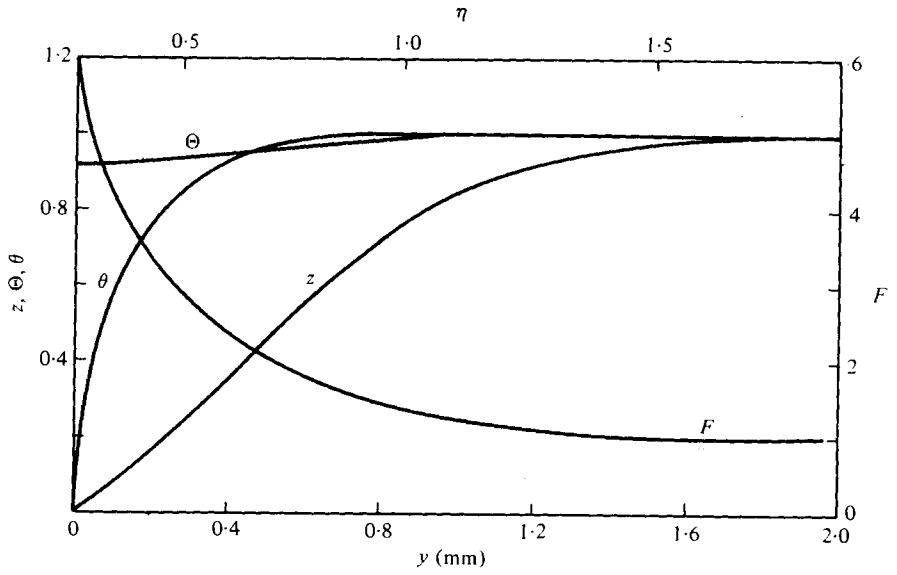

FIGURE 4. Non-equilibrium flow profiles of normalized velocity F, degree of ionization z, atom temperature θ and electron temperature Θ as a function of η or y for the side-wall boundary layer in argon at $x = 9{\cdot}5$ cm, $M_s = 13{\cdot}1$, $p_0 = 5{\cdot}16$ torr and $T_0 = 300$ °K.

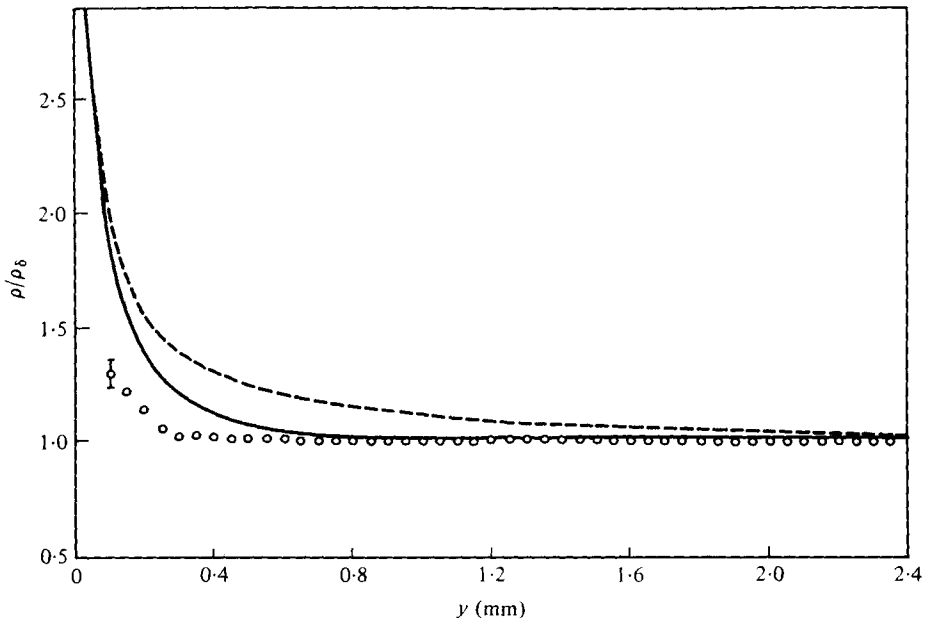

FIGURE 5. Comparison of analytical and experimental profiles of plasma density ρ *vs.* distance y in the side-wall boundary layer in argon at $x = 9{\cdot}5$ cm, $M_s = 13{\cdot}1$, $p_0 = 5{\cdot}16$ cm and $T_0 = 300$ °K. ——, non-equilibrium; – – –, frozen.

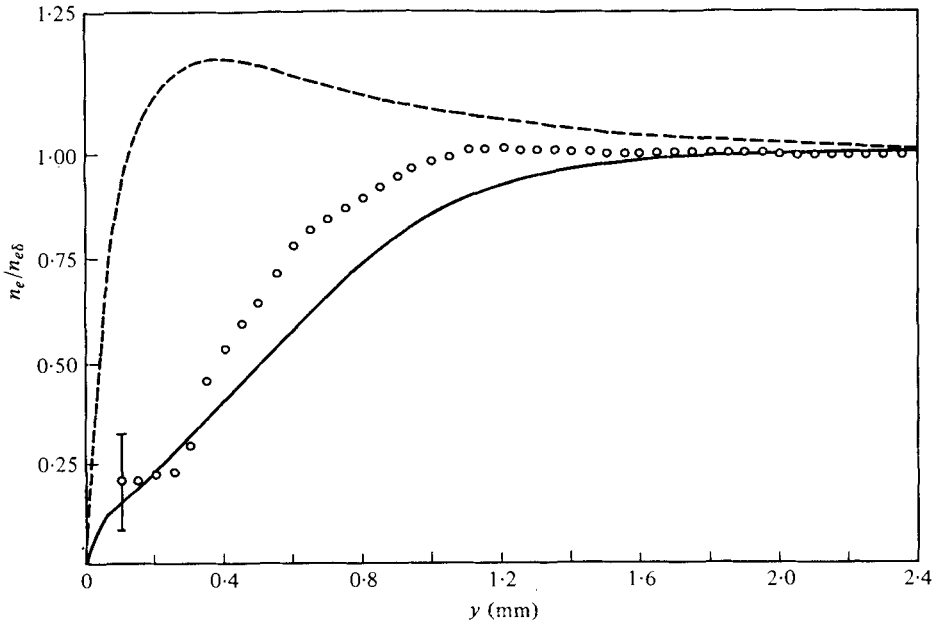

FIGURE 6. Comparison of analytical and experimental profiles of electron number density n_e *vs.* distance y in the side-wall boundary layer in argon at $x = 9{\cdot}5$ cm, $M_s = 13{\cdot}1$, $p_\infty = 5{\cdot}16$ torr and $T_0 = 300$ °K. ——, non-equilibrium; – – –, frozen.

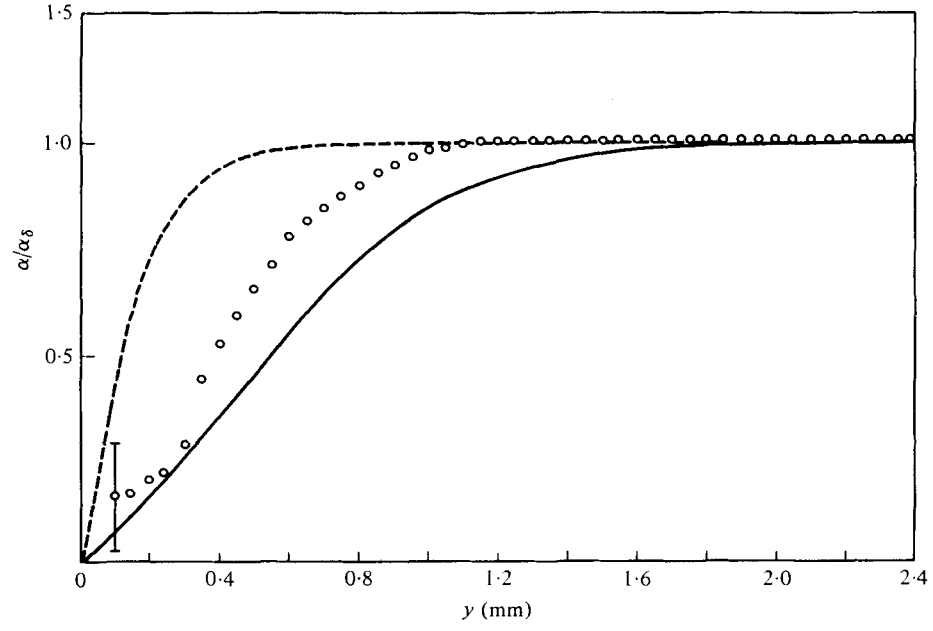

FIGURE 7. Comparison of analytical and experimental profiles of degree of ionization α *vs.* distance y in the side-wall boundary layer in argon at $x = 9{\cdot}5$ cm, $M_s = 13{\cdot}1$, $p_0 = 5{\cdot}16$ torr and $T_0 = 300$ °K. ——, non-equilibrium; – – –, frozen.

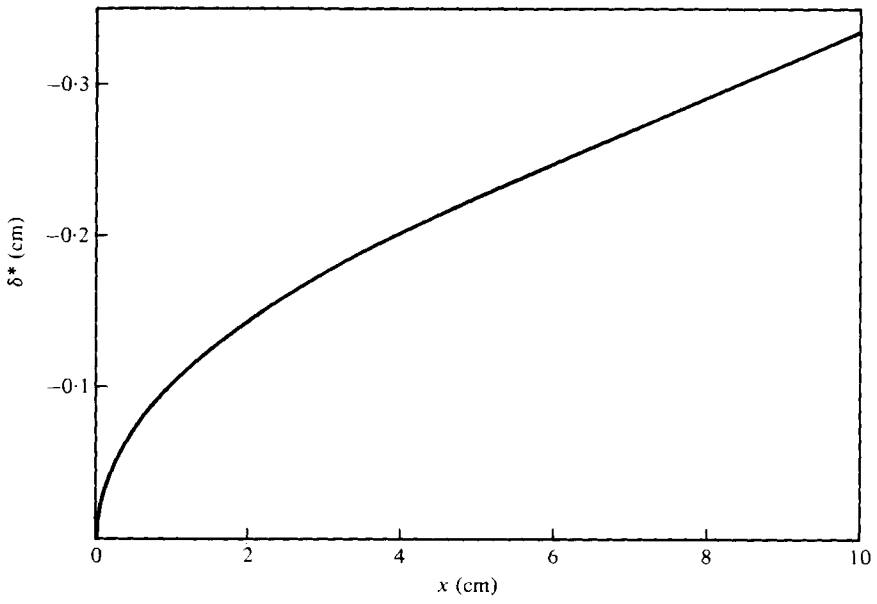

FIGURE 8. Non-equilibrium side-wall boundary-layer displacement thickness δ^* as a function of distance x in argon at $M_s = 13{\cdot}1$, $p_0 = 5{\cdot}16$ torr and $T_0 = 300$ °K.

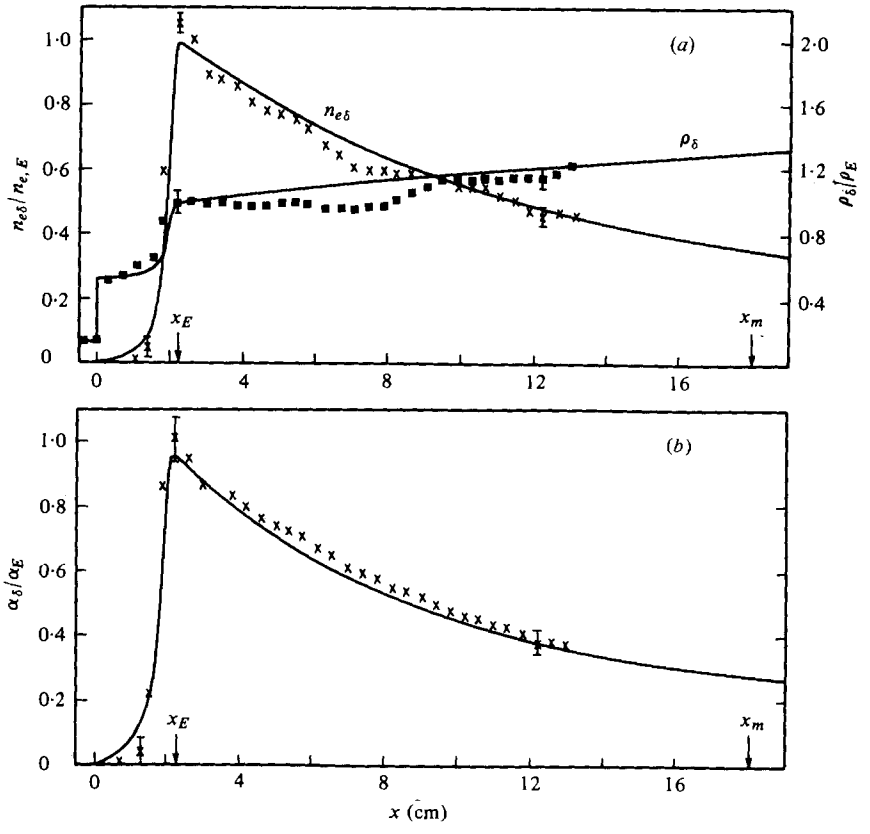

FIGURE 9. Variation of (*a*) ρ_δ and $n_{e\delta}$ and (*b*) α_δ with distance x in the free-stream flow for $M_s = 15{\cdot}9$, $p_0 = 5{\cdot}1$ torr and $T_0 = 298$ °K, $n_{e,E} = 0{\cdot}169 \times 10^{18}$ cm^{-3}, $\rho_E = 0{\cdot}82 \times 10^{-4}$ g/cm^3, $\alpha_E = 0{\cdot}137$.

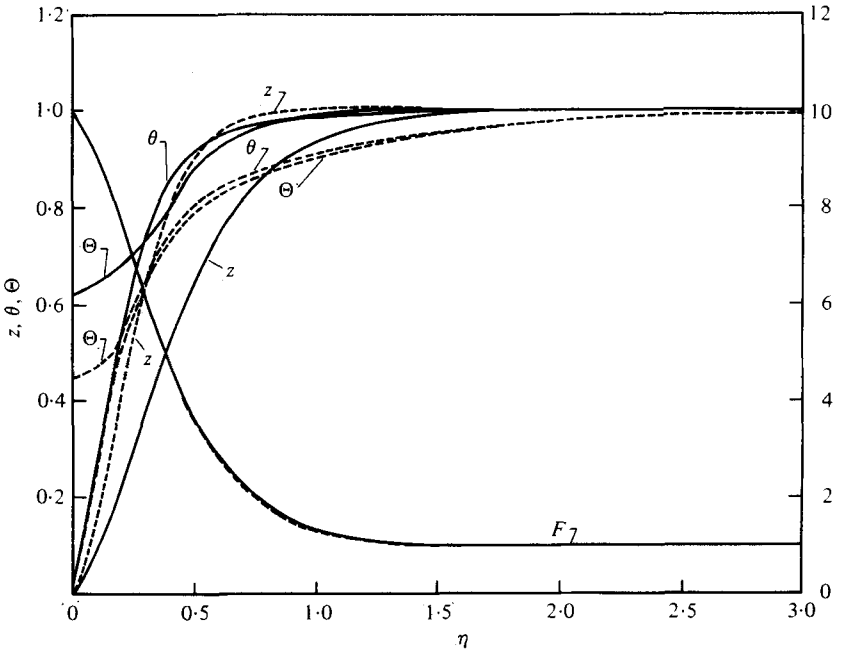

FIGURE 10. Dimensionless non-equilibrium and frozen-flow profiles of velocity F, degree of ionization z, atom temperature θ and electron temperature Θ as a function of η at $x_m = 18$ cm, $M_s = 15{\cdot}9$, $p_0 = 5{\cdot}1$ torr and $T_0 = 298$ °K. ——, non-equilibrium; – – –, frozen.

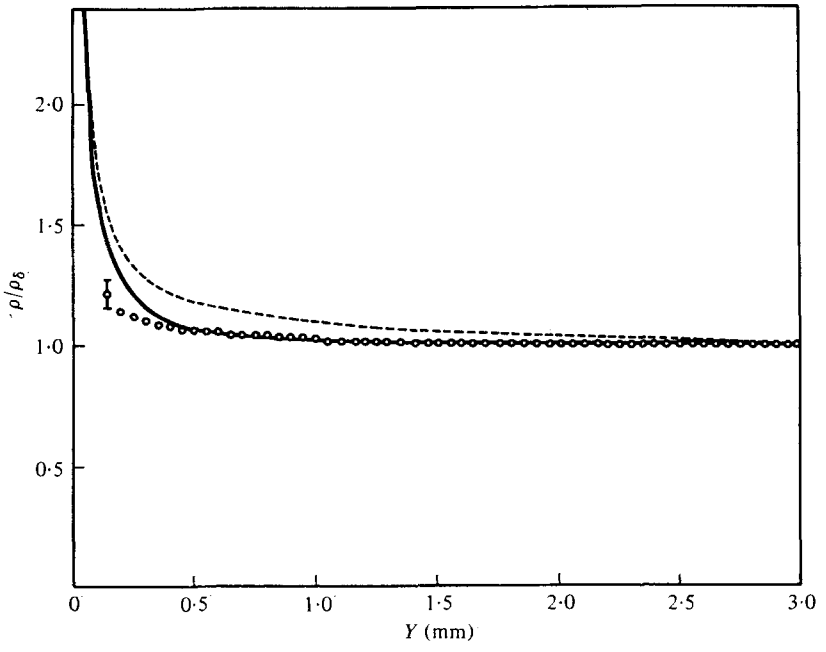

FIGURE 11. Comparison of analytical and experimental profiles of plasma density ρ *vs.* distance y from the wall in the side-wall boundary layer in argon at $x = 18$ cm, $M_s = 15{\cdot}9$, $p_0 = 5{\cdot}1$ torr and $T_0 = 298$ °K. ——, non-equilibrium; – – –, frozen.

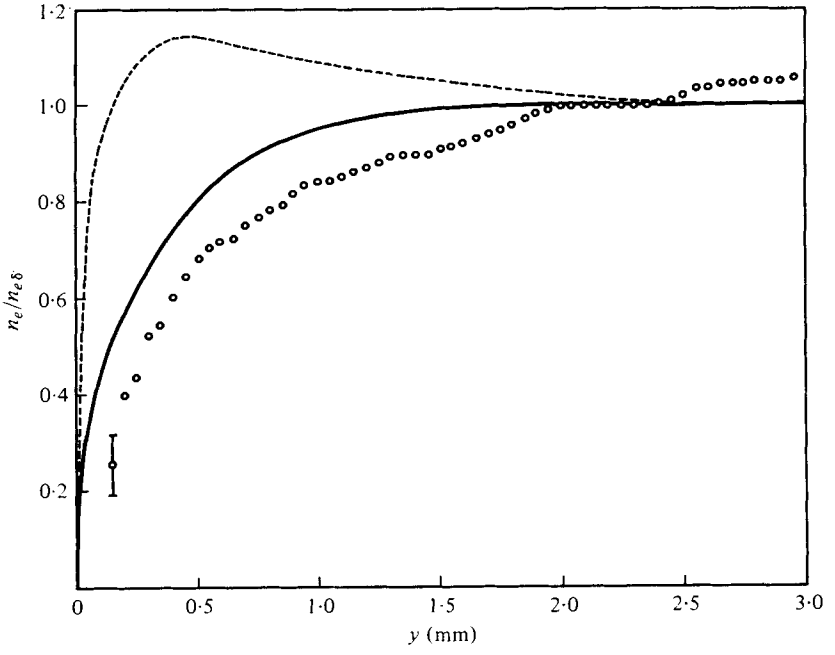

FIGURE 12. Comparison of analytical and experimental profiles of electron number density n_e *vs.* distance y at $x = 18$ cm, $M_s = 15{\cdot}9$, $p_0 = 5{\cdot}1$ torr and $T_0 = 298$ °K. ——, non-equilibrium; – – –, frozen.

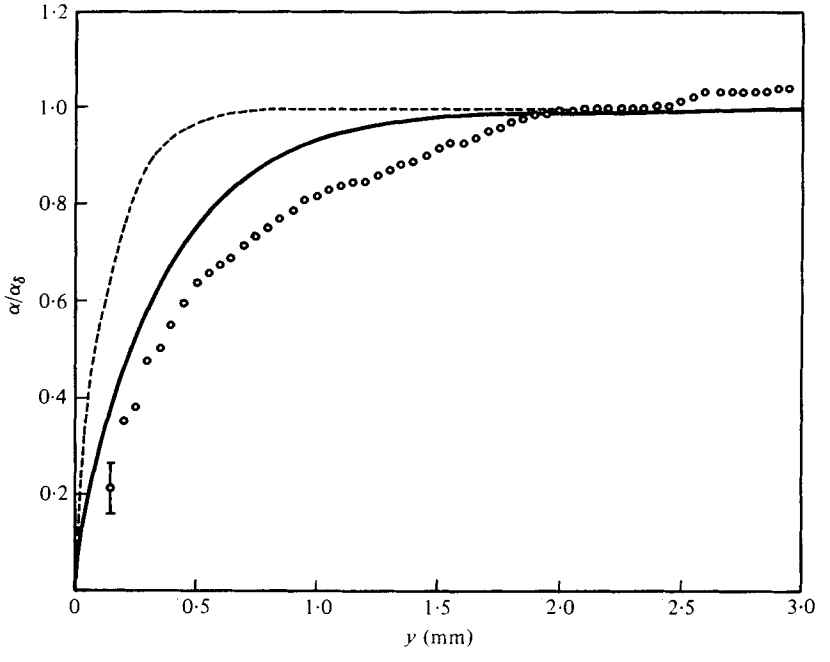

FIGURE 13. Comparison of analytical and experimental profiles of degree of ionization α *vs.* distance y at $x = 18$ cm, $M_s = 15{\cdot}9$, $p_0 = 5{\cdot}1$ torr and $T_0 = 298$ °K. ——, non-equilibrium; – – –, frozen.

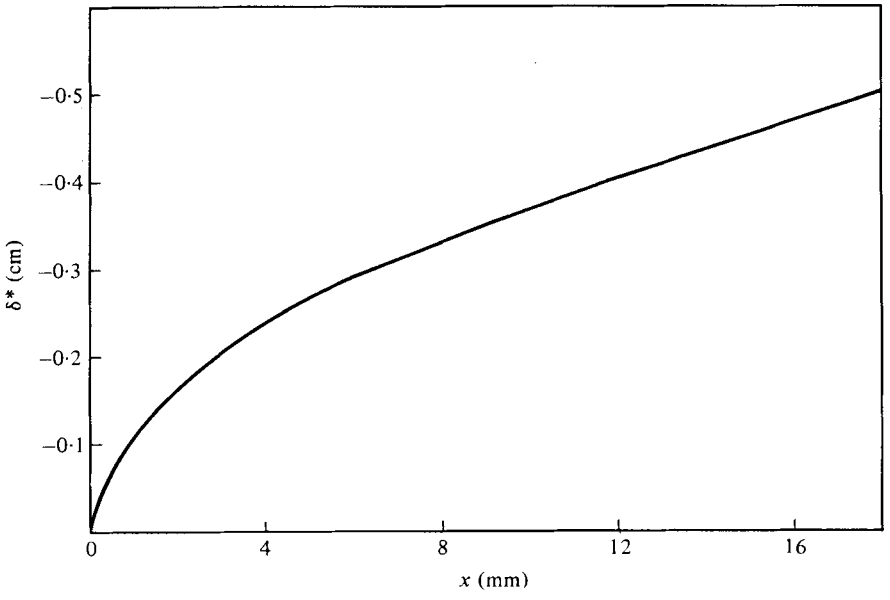

FIGURE 14. Non-equilibrium side-wall boundary-layer displacement thickness δ^* as a function of distance x in argon at $M_s = 15{\cdot}9$, $p_0 = 5{\cdot}1$ torr and $T_0 = 298$ °K.

The dimensionless non-equilibrium flow profiles of velocity F, atom temperature θ, electron temperature Θ and the degree of ionization z are shown in figure 4 for $x_m = 9{\cdot}5$ cm. It is seen that the velocity profile is significantly different from the flat-plate profile f' (figure 17 of Liu *et al.* 1978). The thickness of the electron thermal layer is much smaller than predicted by Honma & Komuro. They indicated a thickness almost an order greater than the present result. It is shown that the thickness of the electron thermal layer is of the same order as the thickness of the viscous layer for the side-wall and flat-plate cases. A similar result was found by Hutten Mansfeld (1976) for a thermal–Rayleigh boundary layer.

A comparison of analysis with experimental data is shown in figures 5–7 for the plasma density, electron number density and degree of ionization, respectively. Much better agreement is obtained between the measured results and the non-equilibrium solutions. The agreement with the frozen solution is rather poor. The boundary-layer displacement thickness δ^* is plotted in figure 8. Owing to the shape of the velocity profile, δ^* is now negative, as expected. It is seen that the displacement thickness increases almost linearly with x when x is greater than 2 cm. A comparison with figure 10 of Liu *et al.* shows that the side-wall boundary layer is about an order of magnitude thicker for an equivalent x owing to the fact that the shock speed is much larger than the free-stream flow velocity in the side-wall case.

The free-stream electron number density $n_{e\delta}$, plasma density ρ_δ and degree of ionization α_δ for case 2 ($M_s = 15{\cdot}9$ and $p_0 = 5{\cdot}1$ torr) are shown in figure 9 together with the experimental results. Good agreement is obtained for the free-stream inviscid flow quantities. It should be noted that, in the radiative-cooling region ($x > x_E$), the particle velocity, electron and atom temperatures and the electron number density all decay gradually owing to radiation-energy losses. The measuring station x_m is far

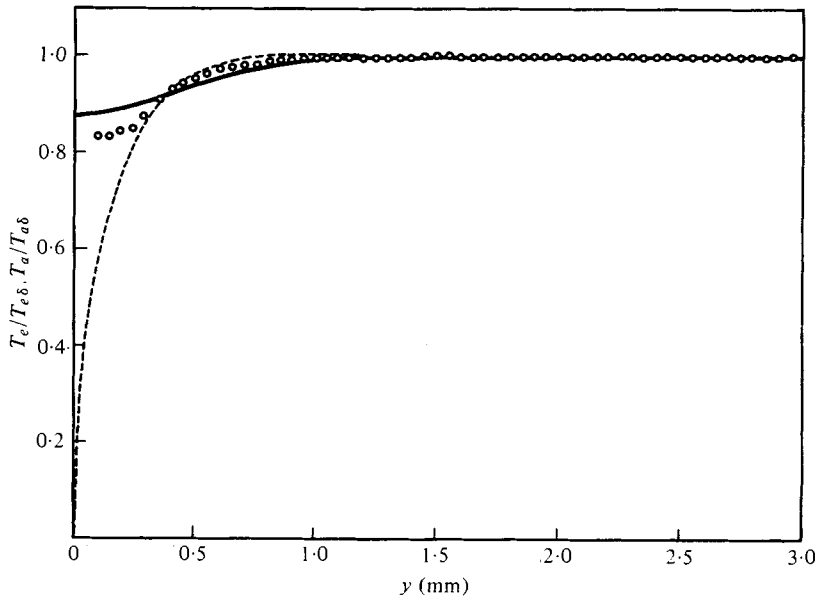

FIGURE 15. Comparison of analytical and experimental profiles of plasma temperatures *vs.* distance y at $x = 9{\cdot}5$ cm, $M_s = 13{\cdot}1$, $p_o = 5{\cdot}16$ torr and $T_0 = 300$ °K. ——, T_e; – – –, T_a.

away from the electron-cascade front at $x = x_E$ and the radiation process plays an important role in the structure of the boundary-layer flow.

The dimensionless profiles of θ, Θ, z and F for non-equilibrium and frozen flows at $x = 18$ cm are shown in figure 10. The chemical reactions have significant effects on all flow profiles except velocity. The analytical and experimental results for the profiles of plasma density and electron number density are compared in figures 11 and 12, respectively, while the corresponding degree-of-ionization profile is shown in figure 13. The experimental results are in even better agreement with the non-equilibrium profiles than in case 1.

Two significant differences can be seen when comparing cases 1 and 2.

(i) The profiles of electron number density (or degree of ionization) for case 2 are overpredicted, while the experimental results lie between the non-equilibrium and frozen solutions for case 1.

(ii) Two-dimensional effects are found in the free-stream flow for case 2 but not for case 1. That is, in case 1 the flow parameters reached their asymptotic values at the edge of the boundary layer. However, in case 2 the flow density and electron number density kept on increasing with distance from the wall and did not reach their asymptotic values.

The reasons for the discrepancies between these two cases can be explained as follows. In the studies of shock-wave structure in ionizing argon and krypton (Glass *et al.* 1977; Glass & Liu 1978), it was found that the electron-cascade front moves in towards the wall to approach the translational shock wave, slowly at first and then very rapidly. Figure 13 of Glass & Liu (1978) shows contours of constant α for shock waves ($M_s = 16{\cdot}5$ and $13{\cdot}6$) moving into pure argon obtained by Brimelow. While similar effects are seen in both instances, the phenomenon is much more prominent for the stronger shock wave. This might have been expected owing

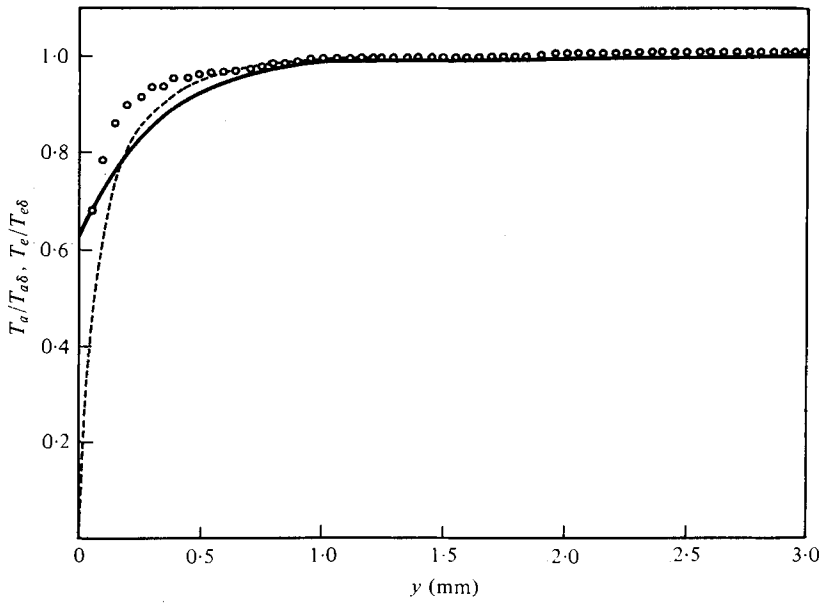

FIGURE 16. Comparison of analytical and experimental profiles of plasma temperatures *vs.* distance y at $x = 18$ cm, $M_s = 15{\cdot}9$, $p_0 = 5{\cdot}1$ torr and $T_0 = 298$ °K. ——, T_e; – – –, T_a.

to the greater electron number density and the shorter relaxation length as in case 2. The reasons for this premature ionization close to the wall are far from clear (Glass & Liu 1978).

The displacement thickness δ^* is plotted in figure 14 as a function of distance x. It should be noted that the slope of δ^* at $x = 2$ cm is changed owing to significant variations in free-stream values at the electron-cascade front. The displacement thickness increases almost linearly with x when x is greater than 3 cm.

Among the commonly used plasma instruments for measuring electron-temperature profiles are Langmuir probes and microwave transmission. However, these methods fail in a flowing high-density and high-temperature plasma. In the present case, an indirect measurement of the plasma-temperature profile inside the boundary layer can be determined from the interferometrically determined profiles of ρ and n_e by use of the assumption of thermal equilibrium. In general, this assumption is crude. However, some interesting data result from a comparison of analytical and experimentally derived plasma-temperature profiles. Figures 15 and 16 show such comparisons for two cases. It is seen that the experimental plasma temperature is in better agreement with the calculated electron temperature than with the atom temperature near the wall. In the outer part of the boundary layer the agreement is good for both temperatures.

It is worth noting that the assumption $\rho_i V_i \approx -D_a(\partial\alpha/\partial y)$ made in the analysis was removed and replaced by

$$\rho_i V_i \approx -D_a\left[1+\frac{T_e}{T_a}\right]\frac{\partial\alpha}{\partial y} \tag{9}$$

in the computer program, where V_i is the ion-diffusive velocity. It is shown that the effects on the flow profiles are very small. This was done to remove instabilities for the side-wall boundary layer by using (9) at the higher shock Mach number.

Comparison between side-wall and flat-plate cases

From the foregoing comparison of analysis and experiment for both side-wall and flat-plate boundary-layer (Liu *et al.* 1978) flows for nearly identical initial conditions, the following differences are observed.

(i) The experimental data and the non-equilibrium analysis show that there is no bump in the n_e profile for the side-wall boundary layer. However, such a bump is observed in the experimental flat-plate boundary-layer profile. The frozen solution predicts a bump for both layers.

(ii) Better agreement is obtained between experiment and the non-equilibrium analysis in the side-wall case, while the frozen solutions agree better with experiment than do the non-equilibrium solution for the flat-plate case.

(iii) More significant differences exist between the analytical non-equilibrium and frozen plasma-density profiles for the side-wall boundary layer, while the difference is small for the flat-plate case.

(iv) Even though the predicted displacement thickness for the side-wall boundary layer is an order of magnitude greater, the predicted and actual density, electron-number-density and degree-of-ionization layers have correspondingly similar values. The density thickness is usually about half the electron-number-density thickness. This shows that the total density is not a sensitive indicator for distinguishing between the types of solution for the boundary layer, whereas the electron-number density profile may be readily used for this purpose.

By and large all analytical profiles are consistent for both types of boundary layer. The fact that the experimental data are in better agreement for the side-wall boundary-layer flow may result from the following.

(i) The unsteady effects on the side-wall boundary layer are smaller than those on the flat-plate boundary layer. In the previous analysis of the flat-plate boundary layer the flow was assumed to be quasi-steady while in reality it varies with time owing to radiation-energy losses and the changes in flow properties caused by the growing side-wall boundary layers. These effects were shown to be more pronounced at high shock Mach numbers, where the radiation-energy losses in the free stream are significant. For example, the agreement between theory and experiment for $M_s = 16{\cdot}6$ is not as good as for $M_s = 12{\cdot}6$ for the n_e and α profiles in the flat-plate cases.

(ii) There is significant non-equilibrium ionization in the free-stream flow in the side-wall case but the flat-plate flow is almost in a state of radiant equilibrium. The variations of the flow properties with distance x have been taken into account in the side-wall case, while these free-stream variations have been neglected in the previous flat-plate calculations in order to satisfy the steady-state condition.

Effects of side-wall boundary layer on shock-wave structure

Our previous analysis (Glass & Liu 1978) of shock-wave structure in ionizing argon was based on the assumption that the flow is one-dimensional. Consequently the effects of the growth of the side-wall boundary layer on the relaxation region were neglected. Enomoto (1973) studied the effects of the side-wall boundary layer on the structure of ionizing shocks in argon. He based his work on Mirels' (1966) results for the side-wall boundary layer of a non-ionizing gas and used only the conservation of mass of the flow mixture. He thus showed that the temperature, density and pressure

increase in value with distance from the shock front owing to the growth of the side-wall boundary layer, and most important, that the ionization relaxation time was significantly shortened.

In general, the effective one-dimensional equations for the flow in a shock tube must be obtained by integrating the three-dimensional flow equations over the entire shock-tube cross-section. These effective one-dimensional equations are functions of the variations of appropriately defined side-wall boundary-layer thicknesses such as displacement, momentum, atom and electron energy, and electron number density along the shock-tube wall. Recent results show that the relaxation length of an ionizing argon shock structure is significantly reduced by the effects of the side-wall boundary layer for $M_s = 13{\cdot}1$ and $p_0 = 5{\cdot}16$ torr case. The results of interactions between inviscid free-stream and side-wall boundary-layer flows in ionizing argon will be reported later.

Finally, from a comparison of the theoretical work of Hutten Mansfeld (1976) with the experimental results of Kuiper (1968) for a thermal–Rayleigh boundary layer, no bump occurred in the n_e profiles. It should be noted that, in Kuiper's experiment with $M_s = 11{\cdot}1$ and $p_0 = 5$ torr, the radiation-energy loss was not very significant. Nevertheless, similar trends of the flow profiles are observed in his end-wall and the present side-wall boundary-layer flows.

5. Conclusions

The complete set of equations for shock-tube side-wall laminar boundary-layer flows in ionizing argon was solved by a six-point implicit finite-difference scheme. The flat-plate and shock-tube side-wall boundary-layer flows were analysed and compared with interferometric data obtained using the UTIAS 10×18 cm Hypervelocity Shock Tube equipped with a 23 cm diameter Mach–Zehnder dual-wavelength interferometer at shock Mach numbers $M_s \sim 13$ and 16 at an initial argon pressure $p_0 \sim 5$ torr.

The agreement between analysis and experiment for the density profiles appears to be good to excellent. The data for a flat-plate boundary layer show a bump in the profiles of electron number density. The unsteady character of the inviscid flow may have an important effect on the flat-plate boundary-layer structure at high shock Mach numbers where the radiation energy is significant.

Better agreement is obtained between the interferometric data for the total density and electron number density and the non-equilibrium analysis for the side-wall boundary-layer flow. No bump is predicted by the theory and none is obtained experimentally for the side-wall case. It is possible that in the future, when better values are available for collision cross-sections, transport properties and the wall electric-sheath boundary conditions, it will be possible to use the interferometric data again to test the validity of the improved analytical results.

From the foregoing studies on the flat-plate and side-wall boundary layers for ionizing argon flows, the following conclusions can be reached:

(*a*) Near the wall the flows are in non-equilibrium or near frozen. Equilibrium solutions are valid only for the flow in the outer part of the boundary layer. The same conclusion was drawn by Knōōs for a side-wall boundary layer and by Hutten Mansfeld for a thermal–Rayleigh boundary layer.

(*b*) The variation of the flow profiles with distance x is different for the two types of boundary layer. For example, the velocity profile is almost independent of x for the

flat-plate boundary layer but not for the side-wall boundary layer. Consequently, similarity assumptions are reasonable for the velocity and atom temperature profiles for the flat-plate case, where the free-stream variations are small, and even for the side-wall velocity profiles. However, large errors will arise in profiles of electron number density and temperature from similarity assumptions in both cases.

(*c*) Unlike the profiles of total number density, the profiles of electron number density are very sensitive indicators for comparing frozen, equilibrium and non-equilibrium analyses with experiments.

(*d*) The thickness of the electron thermal layer is of the same order of magnitude as that of the viscous boundary layer for both flat-plate and side-wall boundary layers. A similar conclusion was drawn by Hutten Mansfeld from a comparison between his analysis and Kuiper's experimental data for a thermal–Rayleigh boundary layer.

The assistance we received from Mr F. C. Tang in evaluating the interferometric data is acknowledged with thanks. The financial assistance received from the U.S. Air Force under Grant AF-AFOSR 77-3303 and from the National Research Council of Canada is gratefully acknowledged.

REFERENCES

BOYER, A. G. 1965 *Inst. Aerospace Stud., Univ. Toronto. Rep.* UTIAS 99.
BREDFELDT, H. R., SCHARFMAN, W. E., GUTHART, H. & MORITA, T. 1967 *A.I.A.A. J.* **5**, 91.
BRIMELOW, P. I. 1974 *Inst. Aerospace Stud., Univ. Toronto Tech. Note* UTIAS 187.
BRISTOW, M. P. F. 1971 *Inst. Aerospace Stud. Univ. Toronto Rep.* UTIAS 158.
BROWN, R. T. & MITCHNER, M. 1971 *Phys. Fluids* **14**, 933.
ENOMOTO, Y. 1973 *J. Phys. Soc. Japan* **35**, 1228.
GLASS, I. I. & LIU, W. S. 1978 *J. Fluid Mech.* **84**, 55.
GLASS, I. I., LIU, W. S. & TANG, F. C. 1977 *Can. J. Phys.* **56**, 1269.
HONMA, H. & KOMURO, H. 1976 *A.I.A.A. J.* **14**, 981.
HUTTEN MANSFELD, A. C. B. 1976 Ph.D. thesis, Eindhoven University of Technology.
KNŌŌS, S. P. 1968 *J. Plasma Phys.* **2**, 207.
KUIPER, R. 1968 *Stanford Univ. Sudaar Rep.* no. 353.
LIU, W. S., WHITTEN, B. T. & GLASS, I. I. 1978 *J. Fluid Mech.* **87**, 609.
MIRELS, H. 1966 *Phys. Fluids* **9**, 1907.
TAKANO, Y. & AKAMATSU, T. 1975 *J. Japan Soc. Aero. Space Sci.* **23**, 126.
TANG, F. C. 1977 *Inst. Aerospace Stud. Univ. Toronto Rep.* UTIAS 212.
TSENG, R. C. & TALBOT, L. 1971 *A.I.A.A. J.* **9**, 1365.
WHITTEN, B. T. 1978 *Inst. Aerospace Stud. Univ. Toronto Rep.* UTIAS.

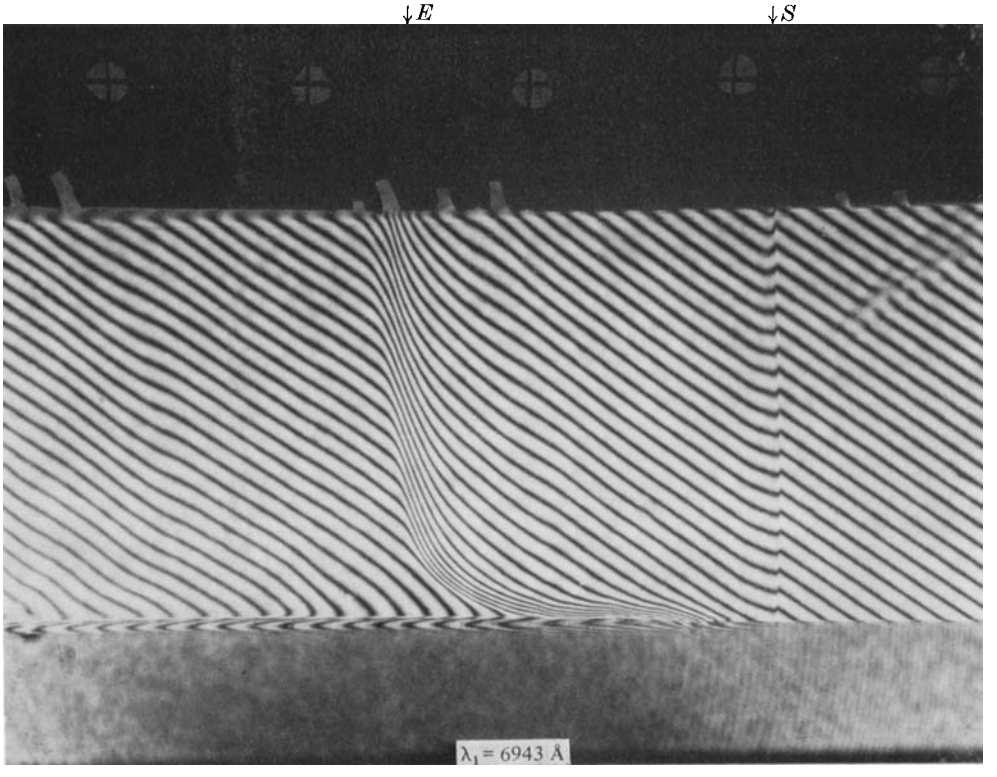

FIGURE 2. Interferogram taken at $\lambda_1 = 6943$ Å of a shock wave moving to the right into argon. $M_s = 15{\cdot}9$, $p_0 = 5{\cdot}1$ torr and $T_0 = 298$ °K. The translational shock-wave front S and the electron-cascade front E are clearly shown; the distance between them is the relaxation zone $x_E = 2{\cdot}1$ cm; cross-wires at 1·0 cm. Note how E approaches S near the wall and the build up of the side-wall boundary layer from S to the left.